Investigation of softening induced indentation size effect in Nanoglass and Metallic glasss

S.S. Hirmukhe [a], A. Sharma [b], Sree Harsha Nandam [c], Horst Hahn [c,d], K.E. Prasad [b], I. Singh [a,*]

[a] Department of Mechanical Engineering, Indian Institute of Technology Indore, Simrol, Indore 453552, India
[b] Department of Metallurgy Engineering and Materials Science, Indian Institute of Technology Indore, Simrol, Indore 453552, India
[c] Institute of Nanotechnology, Karlsruhe Institute of Technology, Hermann-von-Helmholtz-Platz 1,76344 Eggenstein -Leopoldshafen, Germany
[d] Herbert Gleiter Institute of Nanoscience, Nanjing University of Science and Technology, Nanjing, China

ARTICLE INFO

Keywords:
Nanoindentation experiments
Finite element analysis
Nanoglass
Metallic glass
Indentation size effect

ABSTRACT

In this work, binary $Cu_{60}Zr_{40}$ nanoglasses (NGs) and melt spun ribbons (MGs) are synthesized by using magnetron sputtering in an inert gas condensation (IGC) system and standard melt-spinning, respectively. The bonded interface experiments through micro-indentation, and nanoindentation experiments at different peak loads are conducted on both glasses. In addition, complementary finite element (FE) simulations are performed using finite strain viscoplastic constitutive theory for amorphous metals. The bonded interface experiments reveal smooth and almost semi-circular shaped shear bands in MG, while the formation of wavy shear bands is observed in NG. Further, the primary shear band densities in the MG is higher than that in NG, while the plastic zone size below the indenter is larger in the latter than the former. Furthermore, nanoindentation experiments show that the hardness in NGs as well as MGs decreases with increase in indentation depth signifying both alloys exhibiting the indentation size effect (ISE). However, the ISE is found to be more pronounced in MGs than NGs. The FE simulations show that the less pronounced ISE in NGs is due to the slower softening primarily because of higher friction coefficient, μ in them.

1. Introduction

Nanoglasses (NGs), a new class of amorphous alloys, have shown excellent plasticity compared to their metallic glasses (MGs) counterpart [1]. The increase in plasticity is attributed to their unique nano- and microstructure, which typically consists of amorphous interfaces between glassy grains [1–9]. These interfaces exhibit low density [4,6] and excess free volume [10–12], which facilitates nucleation of multiple shear transformation zones (STZs). This, in turn, lead to numerous shear bands (SBs), distributed uniformly throughout the volume of the material resulting in prolonged homogeneous deformation and enhanced ductility in NGs [1,13,14]. Indeed, Wang et al. [1] reported around 17% of plastic strain in Sc-based NGs under tensile loading in contrast to catastrophic failure in MGs with identical composition. Atomistic and continuum simulations performed on NGs have shown that the strength and ductility of NGs can be tailored by tuning the grain sizes [15–19]. Therefore, before deploying these materials in actual applications, a proper understanding of the influence of microstructure of NGs on their mechanical behavior is essential.

In this regard, Nandam et al. [12] performed nanoindentation experiments on $Cu_{50}Zr_{50}$ binary NGs and MGs, and reported smooth indentation load, P vs. depth, h curves (with no noticeable displacement bursts) and high hardness in the former than the latter. They attributed the high hardness of NGs to the presence of Zr rich dense core surrounded by Cu rich interfaces carrying excess free volume. Franke et al. [20] have also reported a higher hardness and reduced modulus in $Sc_{75}Fe_{25}$ NG. On the other hand, the hardness of Ni-based NG thin films [21] and Pd-based NGs [22] are reported to be lower than their MG counterparts. This was rationalized through higher initial free volume in Ni-based NG thin films and the presence of weaker *Pd Pd* metallic bonds in the interfaces of Pd-based NGs. Thus, whether the hardness of binary NGs is higher or lower than their MG counterparts depends on the constituent elements. Until now, the effect of composition of the constituents on the hardness of NGs of a given system has not been explored in detail.

Furthermore, the hardness is frequently observed to decrease with increased indentation load during the indentation experiments equipped with geometrically self-similar pyramidal indenters such as Vickers and

* Corresponding author.
E-mail address: indrasen@iiti.ac.in (I. Singh).

Berkovich, which is commonly referred to as the indentation size effect (ISE) [23]. The ISE in crystalline materials is caused by various factors such as surface roughness [24], the friction between the indenter facets and test sample [25], and strain hardening triggered by the increase in the density of the geometrically necessary dislocations (GNDs) during initial stages of indentation [26]. However, it is a well-accepted fact that the ISE in crystalline materials is mainly governed by the GNDs induced strain hardening. Interestingly, ISE-like behavior has also been observed in bulk metallic glasses (BMGs), which are free from dislocations and exhibit strain softening [27–32]. For example, Wright et al. [33] observed a drop in the indentation hardness of Zr-based BMG with an increase in indentation load, which the authors attributed to the reduction in intrinsic material resistance for SB nucleation with increasing loads.

To explain the ISE in Zr-based BMGs, Lam and Chong [27] and Yang et al. [28] proposed analytical models by adopting the perspective of strain gradient plasticity theory analogous to the Nix-Gao model [26] for crystalline materials. They argued that the concentration of the geometrically necessary flow defects (GNFDs) such as free volume [28] or shear clusters [27] increases with decrease in indentation depth, which causes enhancement in flow stress of the material. However, it is not clear why the flow stress should increase with increase in flow defects.

In contrast to the above studies, Huang et al. [34] showed that the ISE in BMGs can be effectively eliminated by considering the pile-up effect at different indentation loads and hence they deduced that the ISE in BMGs is an experimental artefact. Pang et al. [35] performed nanoindentation experiments on binary $Cu_{50}Zr_{50}$ thin film and reported almost negligible ISE. They applied the proportional specimen resistance (PSR) model to explain the indentation response and concluded that the friction between the indenter facets and the specimen was negligible resulting in negligible ISE in MG thin films. On the contrary, Rauf et al. [36] reported significant ISE in thin films and melt-spun ribbons of $Cu_{50}Zr_{50}$ and $Cu_{64}Zr_{36}$. Thus, the understanding of the mechanics of ISE in MGs is far from complete. Recently, Sharma et al. [37] reported higher ISE in as prepared (AP) than that in annealed (AN) $Cu_{60}Zr_{40}$ NGs. They showed by employing the hypothesis of Steenberge et al. [29] that the different softening characteristic in AP and AN NGs resulted in different ISE in these materials. The work of Sharma et al. [37] suggests that the internal microstructure of NGs has a marked effect on the deformation behavior and hence ISE in them. Given the completely different microstructures of NGs and MGs, the ISE in the former is expected to be significantly different from the latter with identical composition, though it has not been investigated until now. Further, Hirmukhe et al. [38] have shown that the plastic deformation in NGs is more pressure sensitive than MGs due to high pressure sensitivity of interfaces in the former. However, the effect of pressure sensitivity on the ISE in glasses is not investigated and thus, the mechanism governing ISE in NGs and MGs is not well understood. Therefore, the objective of the current work is to develop a mechanistic based understanding of ISE in NGs and MGs having identical composition.

A binary $Cu_{60}Zr_{40}$ NG and melt spun ribbon (referred to as MG throughout the text) are synthesized and the nanoindentation experiments are performed at different peak loads on both the materials. Further, to clearly understand the subsurface deformation behavior, bonded interface experiments are performed using a Vickers indenter. The complementary finite element (FE) simulations of nanoindentation are also performed by employing the finite strain viscoplastic constitutive theory for amorphous metals to elucidate the underlying mechanism governing ISE in NGs. The results show that both the binary $Cu_{60}Zr_{40}$ NGs and MGs exhibit ISE and that the pressure sensitivity of interfaces in NGs has marked an effect on the ISE of NGs.

2. Methodology

2.1. Experimental procedures

$Cu_{60}Zr_{40}$ nanoglasses (NGs) are synthesized by using magnetron sputtering technique in an inert gas condensation (IGC) system, in an environment of Argon and Helium, and at a pressure of 0.3 *mbar*. The detailed process of synthesis by IGC is explained in the work of Nandam et al. [12]. MG ribbons of the same composition are prepared by using standard melt-spinning techniques in a Edmund Buhler machine. In this technique, the molten metal alloy is poured onto a large rotating Cu wheel which condenses in the form of MG ribbon.

The quasi-static nanoindentation experiments are carried out using a Berkovich diamond indenter with a tip radius of 300 *nm*. The area function of the indenter is calibrated using a standard quartz sample. All the experiments are performed under load-controlled mode within the load range of 2 to 8*mN*. The load function consists of loading, holding, and unloading segments with time intervals of 5, 2, and 5s, respectively. The surfaces of samples are carefully polished to a mirror finish using diamond paste. At least 16 indents are taken for each load to get reliable and statistically presentable data. The spacing between the successive indentations is set to be almost ten times of the maximum indentation depth to avoid the interaction of plastic boundaries. The hardness, H and elastic modulus, E are evaluated using unloading curve by following the Oliver-Pharr method [39] using the following equations:

$$H = \frac{P}{A}, \tag{1}$$

$$E_s = \left(1 \quad \nu_s^2\right)\left[\frac{2\sqrt{A}}{\sqrt{\pi}S} \quad \frac{1 \quad \nu_i^2}{E_i}\right]^{-1}, \tag{2}$$

where P and A are the indentation load and contact area, respectively. Further, in Eq. (2) the parameter S is contact stiffness estimated from the slope of unloading curve, and ν is Poisson's ratio. The subscript s and i denotes specimen and indenter under investigation, respectively. The shear band formation around the periphery of the indentation impression is examined using an atomic force microscope (AFM).

Further, the bonded micro-indentation experiments are performed on both the materials using a Vickers indenter to characterize the shear band morphology underneath the indentation. For this purpose, two equal size specimens are taken, and one side of each specimen are polished up to a surface finish of $0.2\ \mu m$. The polished side of the specimens are bonded together using a strong adhesive ("super glue") and allowed to soak for 5-7 hrs. The bonded specimen is cold mounted such that the bonded interface is on the top of mould and is carefully polished to mirror finish. Vickers indentations are performed directly at the interface with maximum applied load of 0.5N such that the impression of indent coincides with the interface. After the experiments, the bonded interface is opened by dissolving the adhesive in acetone and the subsurface deformed morphology is examined using scanning electron microscope (SEM).

2.2. Finite element analysis

2.2.1. Constitutive model

In this work, a finite deformation Mohr-Coulomb type plasticity model proposed by Anand and Su [40] for MGs is employed because it has been shown to capture the deformation behavior of MGs under bending [40], compression [40], tension [40], and indentation [41]. This model assumes that the plastic deformation in amorphous metals occurs by plastic shearing accompanied by dilatation relative to six potential slip systems defined relative to the principal directions of Kirchhoff stress. According to this model, the plastic shear strain in α^{th} slip system evolves as:

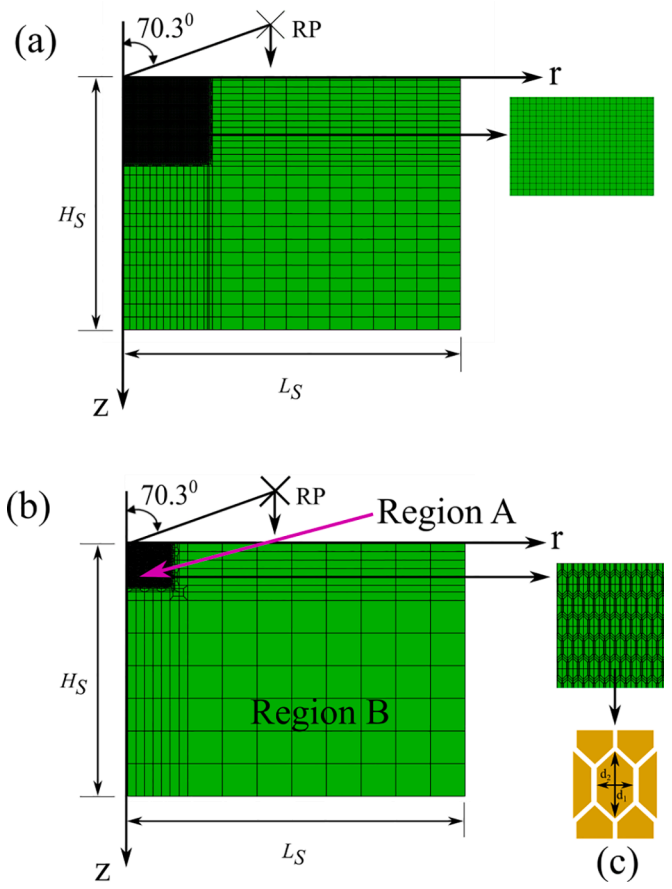

Fig. 1. (a) 2D Axisymmetric FE model of cylindrical specimen along with 'Berkovich equivalent' conical rigid indenter with half cone angle of 70.3^0 employed in indentation simulations of MG and homogenised NG (simulations HNG). (b) Corresponding FE model employed for simulations MNG where microstructure of NG is modelled in a 'Region A', while homogenized NG is considered in 'Region B'. (c) Enlarged view of 'Region A' and a grain whose size is characterized by d_1 and d_2.

$$\dot{\gamma}^{(\alpha)} = \dot{\gamma}_o \left\{ \frac{\tau^{(\alpha)}}{c + \mu\sigma^{(\alpha)}} \right\}^{\frac{1}{m}}, \tag{3}$$

where $m, \dot{\gamma}_o$, and μ are strain rate sensitivity parameter, reference plastic shearing rate, and internal friction coefficient. Further, $\tau^{(\alpha)}$ and $\sigma^{(\alpha)}$ represent the resolved shear stress and compressive normal traction acting on α^{th} slip system. The detailed expression for $\tau^{(\alpha)}$ and $\sigma^{(\alpha)}$ can be found in the work of Anand and Su [40]. Furthermore, in Eq. (3), c is the cohesion, which is assumed to evolve as following to capture the free volume induced softening in MGs:

$$c = c_{cv} + \left(\frac{b}{e \quad 1} \right) \left\{ e^{\left(1 - \left(\frac{\eta}{\eta_{cv}} \right) \right)} \quad 1 \right\}, \tag{4}$$

where, b and c_{cv} are the material constant, while η and η_{cv} are current and saturation level of free volume. The free volume evolution law is given by:

$$\dot{\eta} = \beta \sum_{\alpha=1}^{6} \dot{\gamma}^{(\alpha)}. \tag{5}$$

Here, β is the dilatation function which is assumed to evolve with η as:

$$\beta = \frac{g_0}{e \quad 1} \left\{ e^{\left(1 - \left(\frac{\eta}{\eta_{cv}} \right) \right)} \quad 1 \right\}, \tag{6}$$

where, g_0 is the initial value of dilatancy parameter. The above model has been implemented in the commercially available finite element program ABAQUS 2017 [42] by writing user defined material subroutine UMAT [43,44]. The integration of the constitutive equations is carried out using the implicit backward Euler method.

2.2.2. *Modelling aspects*

The axisymmetric FE simulations on cylindrical specimens are performed using 'Berkovich equivalent' conical rigid indenter having a semi-apex angle of 70.3^0 and spherical tip with radius, R of 300 nm. Fig. 1(a) shows FE discretization of specimen using quadrilateral axis symmetric elements in $r \quad z$ plane along with the rigid indenter. A highly refined mesh is employed below the indenter to capture the distribution of SBs better, while relatively coarser mesh is used in the region away from the indenter. The size of the specimen is chosen as $25R(L_s) \times 20R(H_s)$ to ensure that the plastic zone is well contained beneath the indenter and the boundary effects on indentation response are minimized [38,45]. Further, all the nodes on the left side and bottom edges are restrained from moving along r and z directions, respectively, while a constant displacement rate is applied to the rigid indenter through a reference point RP attached to it (Fig. 1(a)). In this work, two types of indentation simulations are performed on NG, which are referred to as simulation HNG and MNG. In simulation HNG, the microstructure of NG is not modelled, instead the homogenized NG is considered, while discrete glassy grains and interfaces are modelled in simulation MNG (refer Fig. 1(b)). The FE model displayed in Fig. 1(a) is employed for indentation simulations on MGs and simulations on HNG, while the model shown in Fig. 1(b) is used to perform the simulations on MNG. The constitutive behavior of NGs as well as MGs is assumed to be governed by the plasticity theory described in Section 2.2.1.

The values of Young's modulus obtained from nanoindentation experiments on NGs and MGs are used in the corresponding simulations. The values of parameters $\nu, m, \dot{\gamma}_o, g_o, c_{cv}$ and η_{cv} are considered to be identical for MG and NGs (simulations HNG as well as MNG), and these are taken from the work of Anand and Su [40] and Tandaiya et al. [43]. The rationale behind choosing identical values for these parameters are as follows. Like MGs, indentation response of NGs is reported to be also almost strain rate insensitive at room temperature [12], therefore, a lower value of m is considered for both the alloys. Further, Singh et al. [16] argued that the cohesion and free volume distribution should attain approximately the same saturation value at every point inside a shear band that cuts through glassy grains and glassy interfaces in NG. In addition, the free volume and cohesion distribution inside glassy grains in a NG can be assumed to be almost identical to that of MGs used to synthesize them. Therefore, c_{cv} and η_{cv} for MG and NG (glassy grains and glassy interfaces) are also assumed to be identical. The parameter γ_o is a reference strain rate, which is taken to be identical for all the simulations reported in the present study. Further, the initial cohesion c_0 for MG is taken from the work of Lee et al. [46], whereas it is assumed to be 15% lower by choosing lower b for NG (in simulations HNG) than that for MG because of lower yield strength and lower steady state flow stress in the former than the latter with identical composition [1,47]. The values of μ for MGs and NGs (in simulations HNG) are optimised by performing a large number of simulations to get good agreement between the simulated and experimental indentation load versus displacement and hardness versus indentation depth curves. In order to seed defect sites and trigger the shear bands in both NGs (in simulations HNG) and MGs, the initial cohesion is perturbed by 3% [48] about its mean value and randomly assigned to elements.

In the simulation MNG, the microstructure of NG is modelled only in the 'Region A' just beneath the indenter to limit the problem size, while

Table 1
The values of material parameters used for FE simulations of nanoindentation.

Material Parameter	MG	Homogenized NG (HNG)	Microstructured NG (MNG)	
			Grain	Interface
Young's modulus, E (Gpa)	70	120	120	120
Poisson's ratio, ν	0.36	0.36	0.36	0.36
Internal friction coefficient, μ	0.1	0.26	0.1	0.5
Reference plastic shear strain rate, $\dot{\gamma}_o$	0.001	0.001	0.001	0.001
Strain rate sensitive parameter, m	0.02	0.02	0.02	0.02
Constant in cohesion function, b (Gpa)	0.3	0.15	0.3	0.15
Rate of dilatation parameter, g_0	0.04	0.04	0.04	0.04
Plastic volume at saturation, η_{cv}	0.005	0.005	0.005	0.005
Cohesion at saturation, c_{cv} (Gpa)	0.660	0.660	0.660	0.660
Initial cohesion, c_0 (Gpa)	0.960	0.810	0.960	0.810

homogenized NG is considered outside this region, i.e., 'Region B' (refer Fig. 1(b)). The size of 'Region A' is ensured to be sufficiently larger than the plastic zone size below the indenter. Following MD [15,17] and FE simulations on NGs and NG-MG composites [16,38,49], the shape of grains is assumed to be hexagonal whose size is characterized by dimensions d_1 and d_2 along r and z directions, respectively (refer Fig. 1(c)). These values are taken to be 4 and 10 nm, respectively, to achieve an average grain size of 7 nm, which is similar to the size observed in the experiments by Nandam et al. [12], while interface width is taken as1 nm. The materials in 'Region A' and 'Region B' are assumed to follow the constitutive model discussed in section 2.2.1. The values of material parameters considered for 'Region B' are the same as used for simulation HNG (i.e., homogenised NG). Following experimental studies on NGs [4,12], the free volume distribution and chemical composition in grains and the parent MGs used to synthesize NGs are assumed to be identical. Therefore, in simulations MNG, the values of material parameters for grains are taken to be identical to that for MG. Since the glassy interfaces in NGs are characterized by excess free volume [4,12] or lower density [4,6], the initial cohesion is taken to be 15% lower than glassy grains. Further, in order to nucleate shear bands from glassy interfaces, as observed in experiments [1] and MD simulations [15], the initial cohesion is perturbed by 3% about its mean value and randomly assigned to the elements in the interfaces. The value of μ for interface is determined by fitting the simulated indentation load-displacement curve with the experimental data. The values of all the material parameters used in the simulations on MGs, simulations HNG and MNG are listed in Table 1.

3. Results

In this section, the important results obtained from micro-indentation, nano-indentation and finite element simulations are presented.

3.1. Subsurface deformed morphology from micro-indentation experiments

Figs. 2(a) and (b) display the SEM images of subsurface deformation morphology underneath the Vickers indenter at a peak load of 0.5N for MG and NG, respectively. It can be noticed from these figures that shear bands in MG are smooth and almost semi-circular in shape (Fig. 2(a)), while a clear waviness in the shear bands in NG is visible (Fig. 2(b)) which is a consequence of interaction of multiple shear bands promoted by the discrete microstructure (glassy grains and glassy interfaces) in the latter as pointed out by Sharma et al. [50]. Also, the primary shear band densities (number of discrete shear bands) in the MG is higher than that in NG. Further, following Sharma et al. [50] the normalized deformed zone, $\frac{\lambda}{D}$ is calculated for NG and MG, where, λ is the distance of farthest shear band from the tip of indentation impression and D is the distance of the same band from specimen surface (refer Figs. 2(a) and (b)). The ratio $\frac{\lambda}{d}$ is a measure of the plastic zone size, which can be correlated with the sensitivity of plastic flow to the hydrostatic pressure in an amorphous metal [51,52]. Interestingly, it is found that the normalized deformed zone beneath the indenter is around 0.8 for NG, and it is 0.7 for MG. Thus, it can be concluded that *the plastic zone size below the indenter is larger in NG than that in MG,* implying that $Cu_{60}Zr_{40}$ *NG is more pressure sensitive than MG of identical composition*. This will be further confirmed by finite element simulations of nanoindentation in the subsequent section. The trends in the shear band patterns and $\frac{\lambda}{D}$ noticed for $Cu_{60}Zr_{40}$ NG and MG in the present study are in corroboration with the recent subsurface indentation experiment performed on Pd- based NG and MG by Sharma et al. [50].

3.2. Nano-indentation experiments

In Figs. 3(a) and (b), the indentation load-displacement $(P \quad h)$ curves obtained from nano-indentation experiments performed at different peak loads are shown by solid lines for NG and MG, respectively. It can be seen from these figures that the depth of indentation increases with increasing load for both NGs and MGs, but it is lower in the former than the latter for any given load. In addition, it can be seen

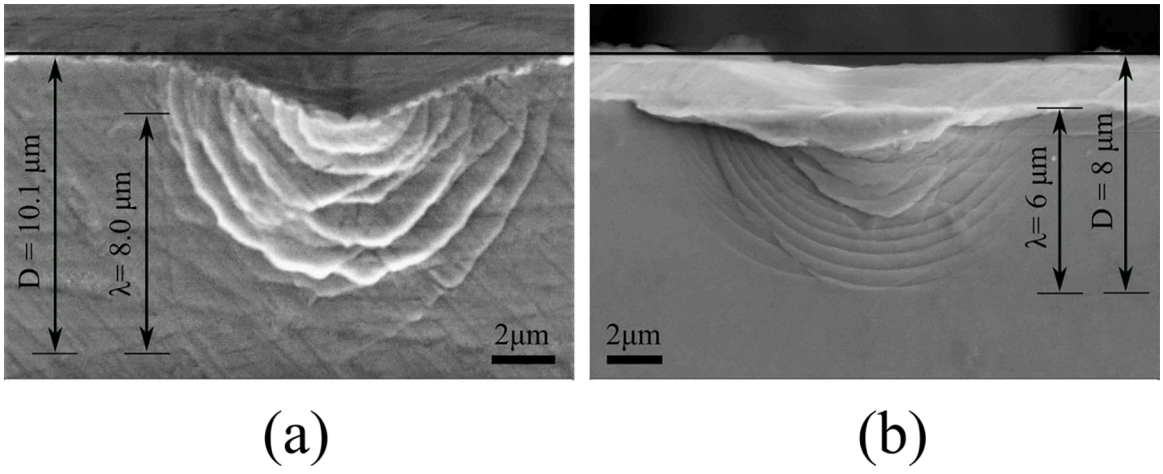

Fig. 2. Scanning electron microscope (SEM) images of the subsurface deformed region at an indentation load of 0.5N for (a) NG and (b) MG.

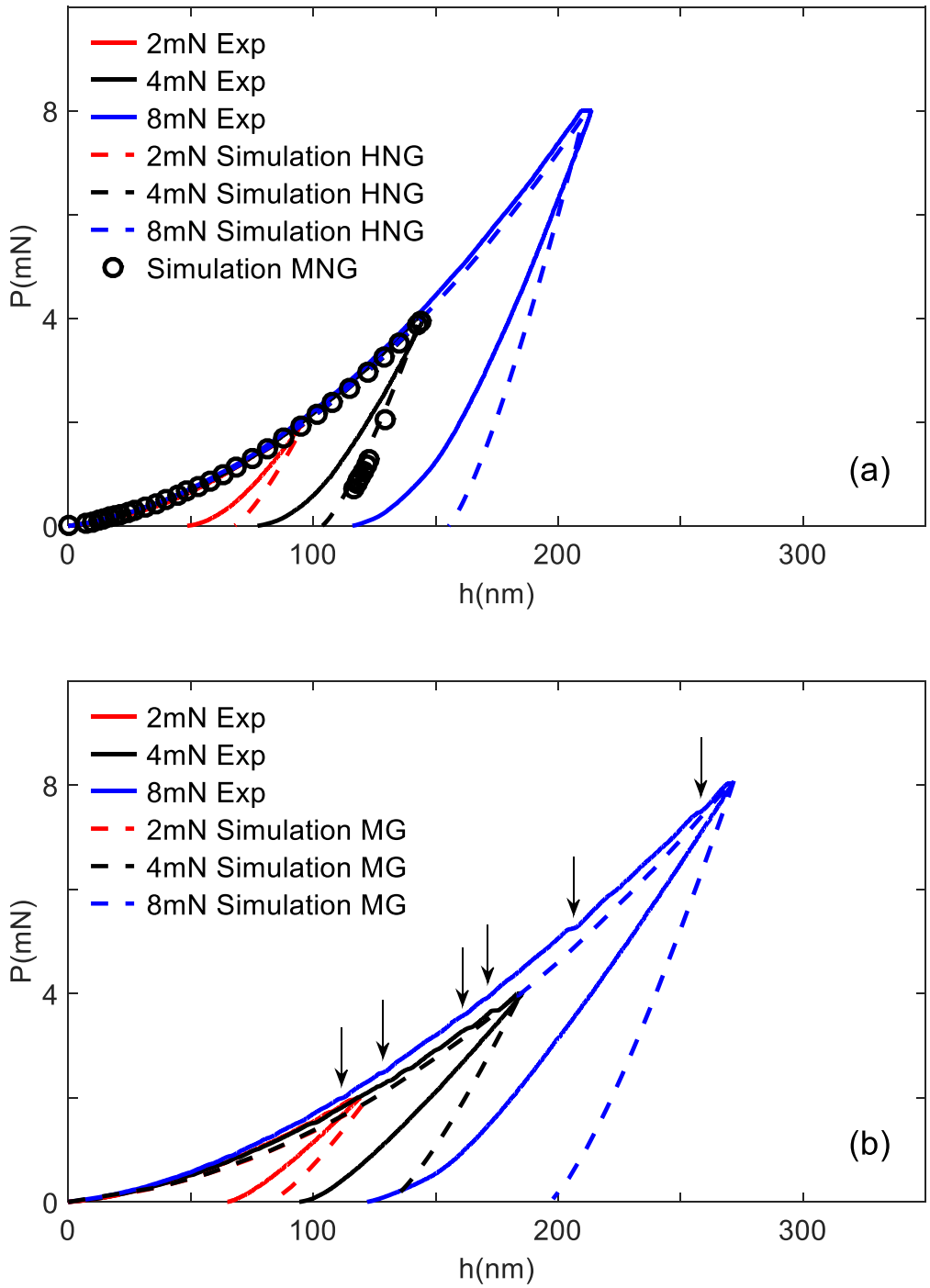

Fig. 3. (a) The indentation load-displacement $(P-h)$ curves corresponding to different peak loads for nanoglasses, NG, obtained from nano-indentation experiments and simulations HNG and MNG. (b) The corresponding curves for metallic glass (MG).

that the elastic recovery in NG is lower than MG suggesting former being harder than the latter of identical composition. Most importantly, no pop-in events are noticed in Fig. 3(a) for any peak load, which signifies almost homogeneous plastic deformation through the nucleation of simultaneous multiple shear bands in NGs. A similar behavior has also been observed in the nanoindentation [1] and experiments [20] as well as atomistic simulations [53,54] of compressive loading on NGs and MGs. On the contrary, many pop-in events are observed in the load-displacement curves of MGs, which are identified by arrows in Fig. 3(b). Note, both the magnitude of the displacement bursts in a pop-in and the number of pop-in events increase with increasing indentation depth. Each pop-in event corresponds to the nucleation and propagation of shear bands underneath the indenter, hence this kind of behavior is termed as localized deformation [1]. A similar finding is reported from indentation studies on BMGs [30,55,56].

In Fig. 4, the variation of nanoindentation hardness, H, determined using Oliver-Pharr method [39], is plotted against maximum penetration depth, h_{max} as shown by solid line curves for NGs and MGs. Note that the indentation hardness decreases with an increase in the indentation depth signifying significant ISE in both the materials. For instance, H for MGs decreases from 6.94 to 5.60 GPa when h_{max} is increased from 118 to 290 *nm* resulting in approx. 19% drop in hardness. A similar trend in H with increase in P or h_{max} has also been reported for Zr-, Pd- based bulk MGs [29,30] as well as for Cu-Zr based MGs [36]

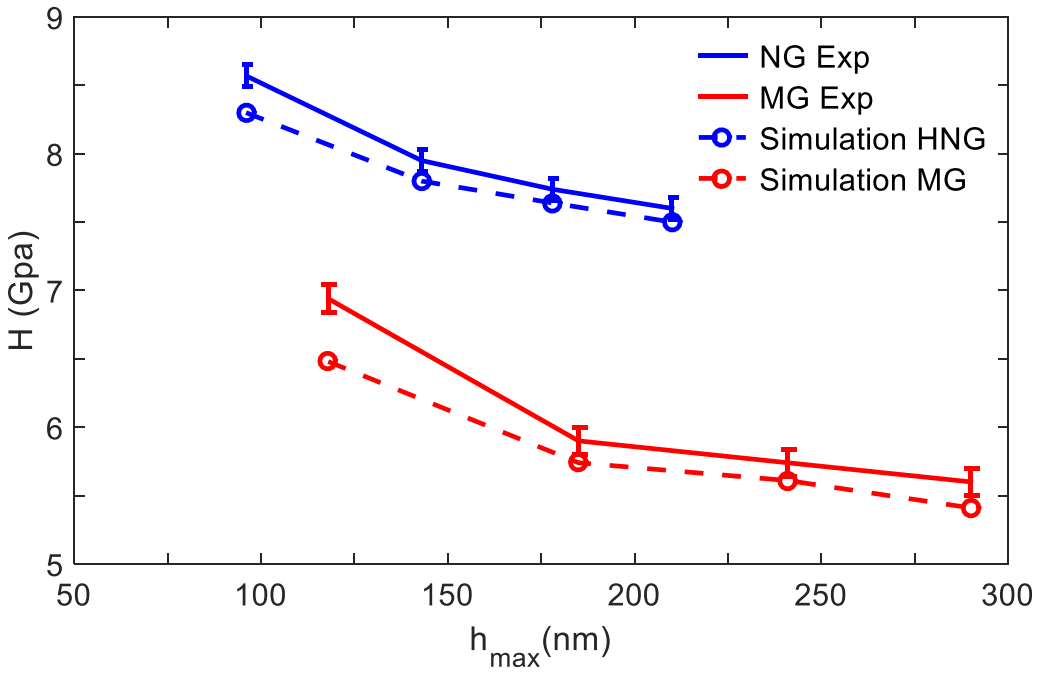

Fig. 4. Dependence of indentation hardness, H calculated at the end of the holding stage, on the maximum indentation depth, h_{max} for NG and MG along with corresponding H values obtained from the FE simulations.

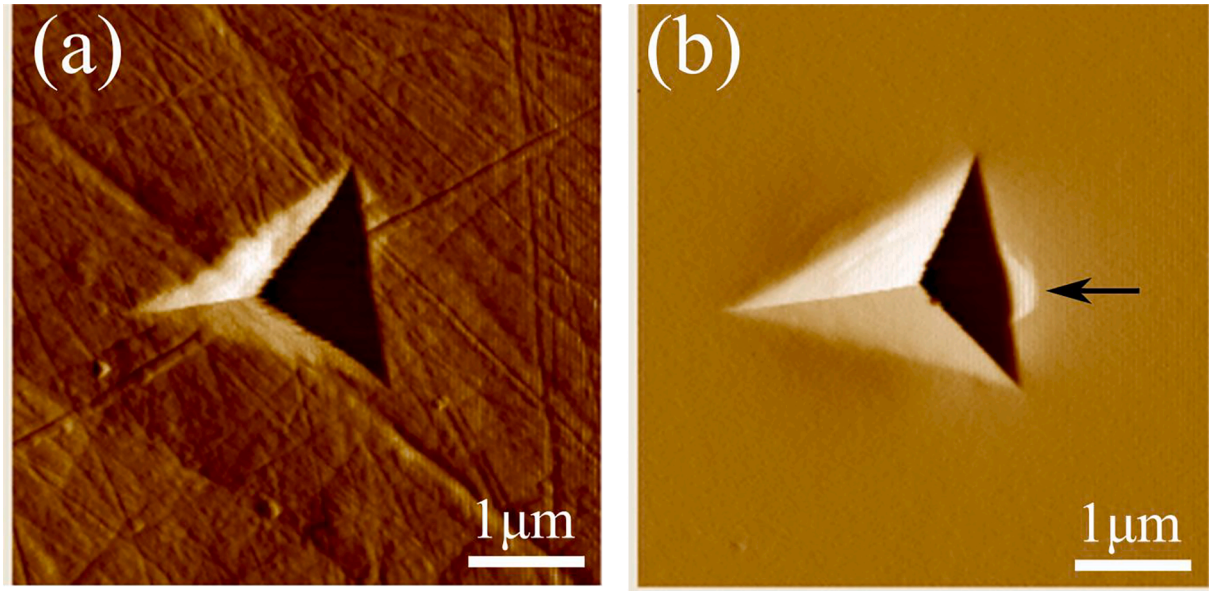

Fig. 5. AFM images of indent corresponding to the peak load of 8mN for (a) NG and (b) MG

during nanoindentation. On the other hand, in the case of NGs, H declines only by 11% with increasing h_{max}, therefore, *it can be concluded that ISE in NGs is less pronounced as compared to MGs*. Recently, Sharma et al. [37] has also reported significant ISE in as prepared as well as annealed NGs.

To understand the plastic deformation around the indent, AFM images of imprints corresponding to the peak load of 8 *mN* are displayed in Fig. 5(a) and (b) for NGs and MGs, respectively. In Fig. 5(a), no shear bands are noticed in the vicinity of the indent confirming plastic deformation is completely accommodated underneath the indentation of NGs. On the other hand, one major SB (marked by arrow) and few minor SBs at the periphery of the impression are noticed in Fig. 5(b) signifying that the plastic flow cannot be completely accommodated in the subsurface deformation zone. The average hardness calculated at the peak load of 8 *mN* for NGs and MGs are 7.59 ± 0.1 GPa and 5.6 ± 0.12 GPa, respectively, and the young's modulus is determined as 120 ± 4 GPa and 70 ± 10 GPa for the former and latter, respectively. Almost similar values for hardness and modulus for as prepared $Cu_{60}Zr_{40}$ NGs have also been reported by Sharma et al [37]. It is noteworthy to mention that higher hardness and Young's modulus in scandium based NGs than MGs has also been reported by Franke et al. [20]. Additionally, recently Nandam et al. [12] performed nanoindentation experiments on $Cu_{50}Zr_{50}$ NGs, and MGs and reported higher hardness and reduced young's modulus in the former than the latter, which they attributed to the presence of heterogeneous structure in NGs.

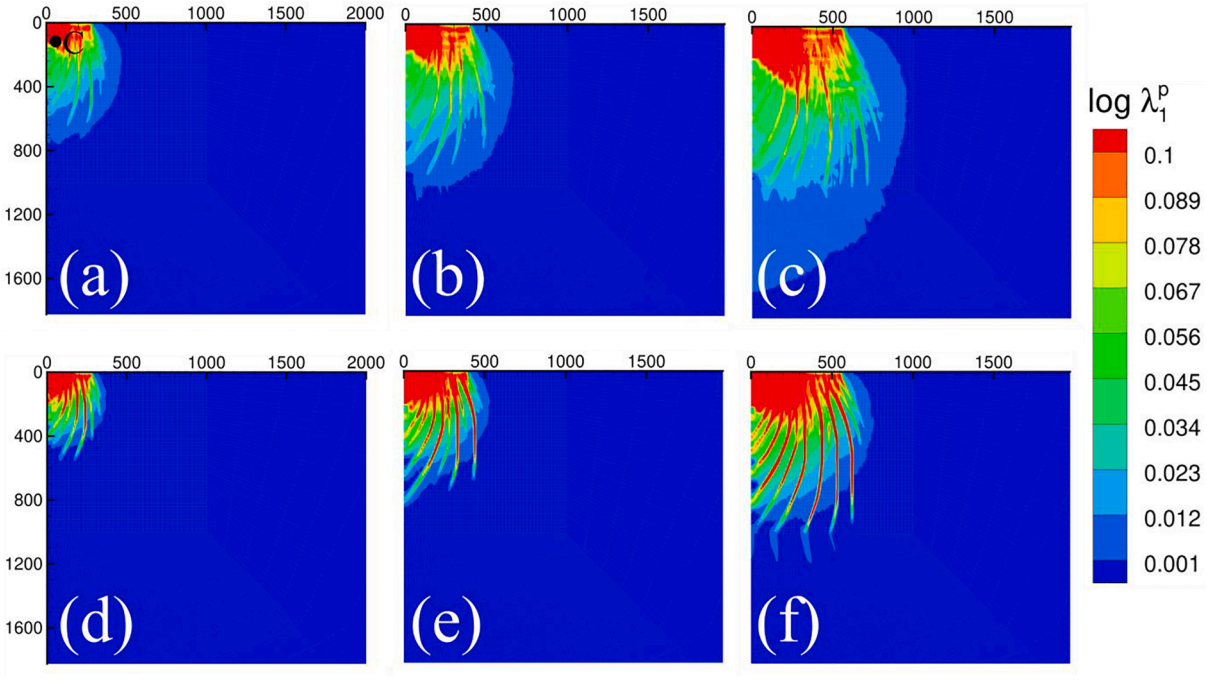

Fig. 6. Contour plots of maximum principal logarithmic plastic strain, $\log\lambda_1^p$ for NG (obtained from simulations HNG) at (a) h 95 nm, (b) h 143 nm and (c) h 210 nm. The corresponding plots for MG are shown in (d)-(f).

3.3. *Finite element simulations of nano-indentations*

The value of μ for MG and NG is optimised to achieve an agreement between the simulated and experimental data to be better than 90%. The simulated P h curves for MG and homogenised NG (HNG) corresponding to the optimum value of μ are displayed by the dashed line in Fig. 3(a) and 3(b), respectively. A good agreement between experiments and simulations of HNG is found for $\mu = 0.26$ (Fig. 3(a)). However, the corresponding curves of MGs give better agreement with the experimental data for a lower value of μ of 0.1 with a marginal difference in the load values at the initial indentation depth (refer Fig. 3(b)). Note that μ for NGs is much higher than that for MGs of identical composition, suggesting indentation response of the former being more sensitive to normal stress than the latter. This observation is in corroboration with the recent study [38], where scandium based NGs are found to be more pressure sensitive than MGs with identical composition. Further, a significant deviation of simulated-unloading curves from the experimental data is observed, which may be due to the increasing nonlinearity in material response during unloading [39]. The values of hardness from FE simulations are plotted against h_{max} by the dashed line in Fig. 4, which shows a good agreement between simulation and experiments for both the alloys, except for the lower indentation depth. The reason for

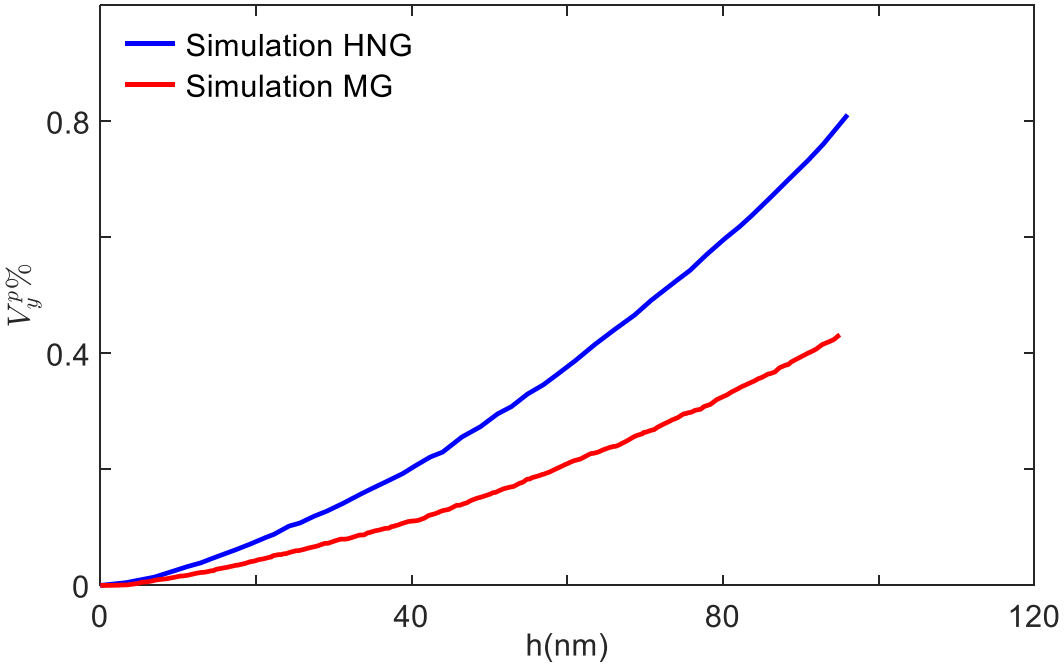

Fig. 7. Variation of volume fraction of plastically deformed material, V_f^p with indentation depth, h for NG (obtained from Simulation HNG) and MG.

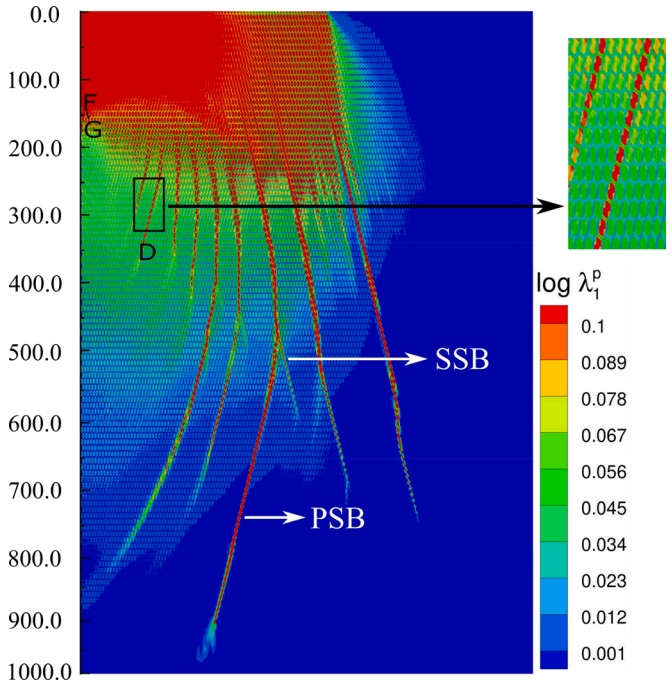

Fig. 8. Contour plot of maximum principal logarithmic plastic strain, $\log\lambda_1^p$ obtained from simulations MNG at h 143 *nm*. The inset figure shows an enlarged view of region D.

this discrepancy will be discussed later in section 4.

In order to understand the evolution of plastic flow underneath the indenter in both the alloys, contour plots of maximum principal logarithmic plastic strain, $log\lambda_1^p$ corresponding to three successive stages of indentation depth, h obtained from simulations on MG and simulations HNG are presented in Fig. 6 in the undeformed configuration. Figs. 6(a)-(c) show the plastic flow distribution in NGs (HNGs) at $h = 95$, 143 and 210 *nm*, respectively, while Figs 6(d)-(f) shows the corresponding plots for MGs at the same penetration depths. It can be noticed by comparing Figs. 6(a) with (d) that discrete bands with higher plastic strain are developed in MGs, while the shear bands are more diffused, and the plastic strain is relatively uniformly distributed in case of NGs. With increasing indentation depth, the number of shear bands, their length and plastic strain inside them increase in both the materials, but strain distribution remains more homogeneous in NGs (refer Fig. 6(b) and (c)) relative to MGs (refer Fig. 6(e) and (f)). In addition, the magnitude of the plastic strain inside the bands in MGs (refer Fig. 6(d-f)) is much higher than the NGs (refer Fig. 6(a-c)). Further, assuming that the plastic deformation at a point would occur if $log\lambda_1^p$ at that point has exceeded beyond 0.001, the volume fraction of plastically deforming material, V_f^p is determined and plotted against h in Fig. 7 for both NG and MG. It can be seen from this figure that V_f^p in NGs is larger than in MGs for identical indentation depth, and it increases more rapidly in the former than the latter. In other words, *the plastic zone size is larger, and it spreads more rapidly in NGs than in MGs, which is a consequence of the higher pressure sensitivity in the former [38]*. Note that the trends pertaining to shear band patterns and plastic zone size for MG and NG displayed in Fig. 6 and 7 are in line with the experimental observations in Fig. 2.

Further, recent FE simulations of nanoindentation on Sc-based NG and MG performed using an extended Drucker-Prager (EDP) plasticity model have shown that the former exhibits higher pressure sensitivity due to the presence of interfaces. It should be mentioned that though the EDP model is pressure sensitive, it cannot capture free volume induced softening, a most important characteristic of amorphous metals. Therefore, the simulation MNG is conducted by modelling the microstructures of NG to determine μ for the interfaces. The value of μ for interface is determined to be 0.5 by fitting the simulated P h curve with experimental data (refer Simulated P h curve of MNG in Fig. 3 (a)). To get more insights on the role of interfaces on the formation of shear bands underneath the indenter, the contour plot of $log\lambda_1^p$ at $h =$ 143 *nm* obtained from simulation MNG is shown in Fig. 8. The profuse shear banding giving the impression of almost uniform distribution of plastic strain just below the indenter is observed, whereas, away from the indenter, multiple discrete shear bands seem to have developed. A close observation of the zoomed-in view of a shear band shows that the amorphous grains with large plastic strain have aligned in the form of a band but strain levels inside interfaces are less than 5%. Thus, the amorphous interfaces prevent the strain localization in a band, consequently the bands in Fig. 8 are not well connected. Fig. 8 also displays the formation of secondary shear bands (SSB) bifurcating from primary shear bands (PSB) (refer bands PSB and SSB in Fig. 8). The formation of secondary shear bands beneath the indenter has also been reported in recent indentation experiments on Pd-based binary NG [50].

4. Discussion

The present experiments show the presence of ISE in MG and NGs, as evident from Fig. 4. Rodriguez et al. [57] showed from experiments and complementary FE simulations on different amorphous materials that the effect of pile-up in hardness values estimated using Oliver-Pharr scheme will be significant if the ratio of elastic energy W_e to total energy, W_t obtained from P h curve is less than 0.5. In order to verify the applicability of the Oliver-Pharr method in the present study, the ratio $\frac{W_e}{W_t}$ is determined at different peak loads and found to be around 0.51 and 0.54 for NGs and MGs, respectively. Therefore, it can be concluded that the ISE of hardness obtained from present experiments is not an experimental artefact but represents a true response of the material.

Jang et al. [23] correlated the hardness of MGs at an applied load with the volume of the material undergoing plastic deformation, and hence, with the activities of STZs and shear bands beneath the indenter. They argued that the volume of the material where plastic deformation has occurred is smaller at lower loads resulting in lesser activities of STZs and fewer shear bands below the indenter, but it enhances with increasing load causing more softening and lesser hardness at higher loads. Steenberge et al. [29] also looked into ISE in MGs as a consequence of rapid softening induced by fast accumulation of free volume during indentation. For this purpose, they correlated the hardness in an amorphous metal with the shear strain rate, $\dot{\epsilon}$, and the concentration of free volume, η using the flow equation of Spaepen [58] and Argon [59] as:

$$H = \frac{6\sqrt{3}k_BT}{\Omega}\ \mathrm{Sinh}^{-1}\left(\frac{\dot{\epsilon}}{2\nu\Delta f\eta}\exp\left(\frac{\Delta G}{k_BT}\right)\right). \tag{7}$$

Here, k_B, T, Ω, ν, Δf, ΔG are Boltzmann constants, test temperature, atomic volume, frequency of atomic vibration, volume fraction of material having potential jump sites, and activation energy, respectively. For load-controlled indentation experiments, the strain rate $\dot{\epsilon} = 1/h(dh/dt)$ underneath the indenter drops rapidly with increase of h and eventually saturating at larger h. The saturation level of $\dot{\epsilon}$ was almost identical for all maximum applied loads [29] and hence it was concluded that the drop of H in MG is mainly due to the enhancement of η during indentation [29,51]. The variation of $\dot{\epsilon}$ in NGs and MGs for the present indentation experiments is plotted against h in Fig. 9(a), which also shows almost an identical drop of $\dot{\epsilon}$ for both materials, irrespective of applied load. Also, the value of $\dot{\epsilon}$ at h_{max} for any load is almost similar. Thus, Eq. (7) suggests that the difference of ISE in NG and in MG should be due to the difference in rate of free volume evolution in both the alloys. To estimate the free volume generation and subsequent softening during indentation, Eq. (7) can be further simplified as [31]:

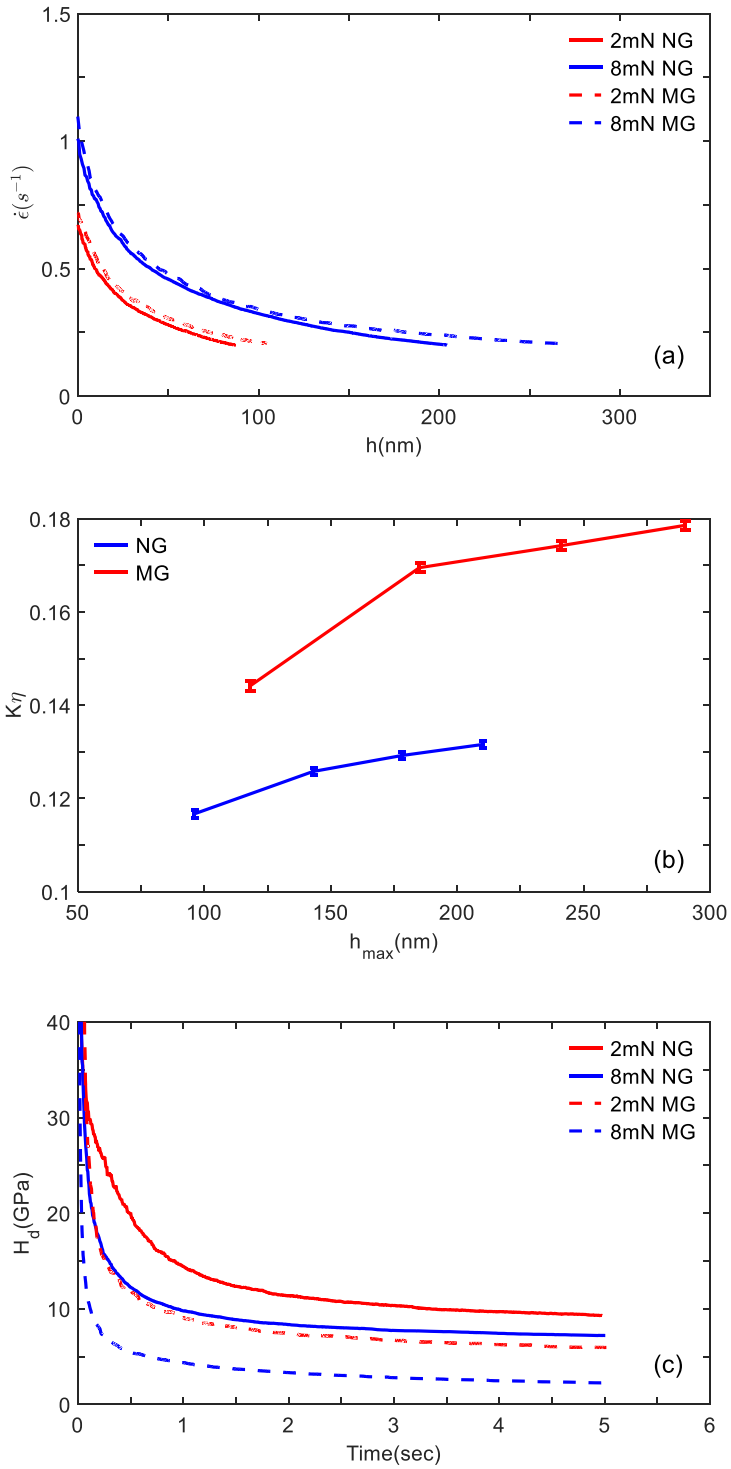

Fig. 9. (a) Variation of shear strain rate underneath the indenter in NG and MG during indentation. (b) Variation of $K\eta$ with h_{max} for MG and NG. (c) The evolution of dynamic hardness, H_d during loading stage of indentation for NG and MG.

$$K\eta = \left(\frac{\nu \Delta f \left(\frac{\Omega}{k_B T}\right) \exp\left(\frac{\Delta G}{k_B T}\right)}{3\sqrt{3}\dot{\epsilon}} \right) \eta = \frac{1}{H} \tag{8}$$

The $K\eta$ versus h_{max} plots displayed in Fig. 9(b) suggest that the free volume increases in both MG and NGs during indentation causing both the alloys to exhibit ISE. Most importantly, enhancement in free volume is faster in MG than NG resulting in rapid softening thereby leading to faster drop in flow stress in the former than the latter. This, in turn, results in faster drop in the hardness of MG than NG.

The difference in free volume generation in NGs and MGs during the indentation experiments can be further confirmed by monitoring the dynamic hardness, H_d, defined as the ratio of instantaneous force to the instantaneous projected contact area [29,57]. By taking the instantaneous projected area as $24.65h^2$ for Berkovich indenter [39] and employing the Oliver-Pharr method [39,60] the evolution of H_d is computed from the loading part of P h curves corresponding to different peak loads for NG and MG, which is displayed in Fig. 9(c). It

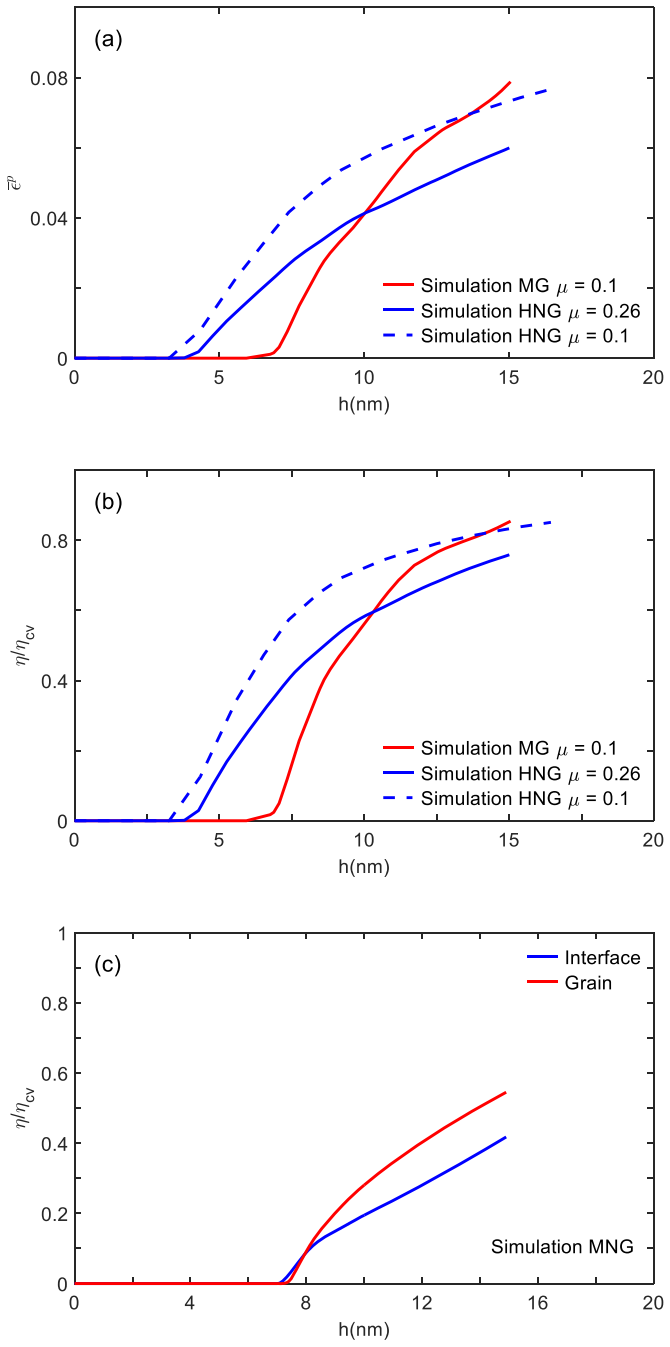

Fig. 10. The variation of (a) Equivalent plastic strain, $\bar{e}^p$ and (b) Normalized free volume, $\frac{\eta}{\eta_{cv}}$ with respect to indentation depth, h at point 'C' taken at z $0.5R$ (refer Fig. 6) for NG (HNG) and MG. (c) The variation of $\frac{\eta}{\eta_{cv}}$ with h inside a grain, F and interface, G marked in Fig. 8 obtained from simulations MNG.

can be noticed from this figure that irrespective of peak load, H_d drops with time and levels off at sufficiently longer time for both alloys. It is important to note that H_d drops more rapidly and saturates to a lower value in MG than that in NG, which signifies a larger amount of free volume being generated during plastic deformation in the former than the latter [29]. The larger free volume will cause more softening and hence a higher drop in hardness leading to more pronounced ISE in MG [29]. Thus, Fig. 9 and Eq. (7) suggest that the faster softening in MG than NG is the primary reason for higher ISE in the former. It should be mentioned that the flow equation used in the analysis of Steenberge et al. [29] does not account for the effect of hydrostatic pressure or normal stress, which is an important characteristic of the plastic deformation in amorphous metals [38,45].

In order to understand the effect of μ on the softening underneath the indenter, the evolution of equivalent plastic strain, $\bar{e}^p$ and free volume η at a point 'C', taken at a depth of $0.5R$, (refer Fig. 6) is recorded from simulations on MG and HNG and plotted against h in Figs. 10(a) and (b), respectively. Due to lower initial cohesion, yielding begins at the early stages of indentation causing plastic strain to evolve earlier in NG, but the rate of enhancement in plastic strain is higher in MG than NG in Fig. 10(a). This, in turn, results in faster free volume generation in MG than NG, as evident from Fig. 10(b) (also refer Eq. (5)). Consequently, MG exhibits relatively rapid drop in cohesion (i.e., softening) in comparison to NG during initial stages of indentation as can be understood from Eq. (4). The slower softening in NG observed in the present simulations is caused by two factors. First, initial cohesion in NG is lower while saturation cohesion is identical to that of MG, consequently, drop in cohesion in NG is slower (see Eq. (4)). Secondly, the higher μ for NG should reduce the shear strain rates, which would result in slower evolution of free volume and slower drop in cohesion (refer Eq. 3-5). In order to contrast the influence of these two factors on the evolution of free volume, one simulation on NG (simulation HNG) is performed by setting μ identical to that used in simulations for MG. The evolution of plastic strain and free volume at point same C obtained from this simulation are displayed by dashed line in Fig. 10(a) and (b), respectively. Note from these figures that the rate of evolution of plastic strain and free volume increases when μ is reduced from 0.26 to 0.1, though it remains slightly lower than the MG. Therefore, *it can be concluded that the softening in NG during indentation is significantly influenced by their sensitivity to the normal stress (i.e., μ). In other words, slower softening caused by the higher μ is an important factor to be considered to explain the lesser ISE in NG than their MG counterpart.*

In order to understand the role played by interfaces on overall softening on NGs, the evolution of free volume inside a grain and interface marked by Points F and G, respectively, taken at a depth of around $0.5R$ (see Fig. 8), is extracted from simulations MNG and compared in Fig. 10 (c). This figure shows that the rate of free volume generation inside interfaces is slower than that in grains. This is a result of the fact that μ for interface is much higher than that for grains, which results in slower strain rate and hence slower growth in η in the former than the latter (refer Eq. (5)). Consequently, cohesion drops slowly (refer Eq. 4) leading to slow softening inside interfaces. This, in turn results in, slower softening in an aggregate NG (considering both grain and interface) and lesser ISE.

It should be mentioned that a significant gradient in η below the indenter has been noticed in the present FE simulations for lower h, which vanishes when h is increased. The presence of a free volume gradient would give rise to interaction stresses between flow defects such as STZs [61]. The interaction stress developed around the curved surfaces such as notches in nanometer-sized MG specimens imparts considerable strain hardening [62]. Since there would be a considerable curvature in the indent impression, therefore, strain hardening promoted by interaction stress during shallow indentation is expected to influence ISE in MGs and NGs. It should be mentioned that the plasticity model employed in the present FE simulations is local and the stress arising due to a free volume gradient is not incorporated in it. This is one of the reasons for significant discrepancy between experimentally measured hardness and the corresponding FE predictions in Fig. 4 for lower h_{max}.

5. Conclusion

In this study, binary $Cu_{60}Zr_{40}$ NGs and melt spun ribbons, (MGs) are synthesized. Micro-indentation as well as nanoindentation experiments are performed on both the alloys. In addition, complementary finite element (FE) simulations of indentations are performed by employing the finite strain viscoplastic constitutive theory for amorphous metals. The important conclusions are as follows:

- SEM images of micrographs obtained from the bonded interface experiments show that shear bands in MG are smooth and almost semi-circular in shape, while wavy shear bands form in NG. Further, the primary shear band densities in the MG are higher than that in NG. However, the plastic zone size below the indenter is larger in NG than that in MG.
- The AFM imaging of impressions generated through nano-indentation reveals almost homogeneous plastic deformation around the indent in NGs, while it shows discrete shear bands for MG.
- NGs exhibit almost smooth indentation load, P vs. depth, h curves, while MGs show serrated curves. The hardness, H of NGs is higher than MGs for all the applied loads, and it decreases more rapidly with increase in P in the latter than the former. Thus, the indentation size effect (ISE) in MG is more profound than that in NG.
- The less pronounced ISE in NG than MG is caused by the slower free volume generation leading to slower softening during indentation in the former than the latter. The FE simulations show that the value of friction coefficient, μ for NG is higher than MG due to higher μ for interfaces in the former. Also, the higher μ retards the free volume generation and hence softening resulting in less pronounced ISE in NG.

Declaration of Competing Interest

The authors declare that they have no known competing financial interests or personal relationships that could have appeared to influence the work reported in this paper.

Acknowledgement

IS would like to gratefully acknowledge the Science and Engineering Research Board (Grant no. SRG/2019/000034 Government of India) for financial support under the SRG Fellowship scheme. We would like to thank Prof. U. Ramamurty, NTU Singapore, and Dr. Abhishek Chaturvedi, IISc Bangalore, for access to nanoindentation test facility. S.H.N and H.H would like to thank the DFG/SPP 1594 program for funding the project under HA1344/30-1 and HA1344/38-1.

References

[1] X.L. Wang, F. Jiang, H. Hahn, J. Li, H. Gleiter, J. Sun, J.X. Fang, Plasticity of a scandium-based nanoglass, Scr. Mater. 98 (2015) 40–43, https://doi.org/10.1016/j.scriptamat.2014.11.010.
[2] J. Jing, A. Kramer, R. Birringer, H. Gleiter, U. Gonser, Modified atomic structure in a Pd-Fe-Si nanoglass, J. Non. Cryst. Solids. 113 (1989) 167–170, https://doi.org/10.1016/0022-3093(89)90007-0.
[3] H. Gleiter, Nanoglasses: A new kind of noncrystalline materials, Beilstein J. Nanotechnol. 4 (2013) 517–533, https://doi.org/10.3762/bjnano.4.61.
[4] J.X. Fang, U. Vainio, W. Puff, R. Würschum, X.L. Wang, D. Wang, M. Ghafari, F. Jiang, J. Sun, H. Hahn, H. Gleiter, Atomic structure and structural stability of Sc75Fe25 nanoglasses, Nano Lett 12 (2012) 458–463, https://doi.org/10.1021/nl2038216.
[5] N. Chen, R. Frank, N. Asao, D.V. Louzguine-Luzgin, P. Sharma, J.Q. Wang, G. Q. Xie, Y. Ishikawa, N. Hatakeyama, Y.C. Lin, M. Esashi, Y. Yamamoto, A. Inoue, Formation and properties of Au-based nanograined metallic glasses, Acta Mater 59 (2011) 6433–6440, https://doi.org/10.1016/j.actamat.2011.07.007.
[6] N. Chen, D.V. Louzguine-Luzgin, G.Q. Xie, P. Sharma, J.H. Perepezko, M. Esashi, A. R. Yavari, A. Inoue, Structural investigation and mechanical properties of a representative of a new class of materials: Nanograined metallic glasses, Nanotechnology (2013) 24, https://doi.org/10.1088/0957-4484/24/4/045610.
[7] C. Guo, Y. Fang, B. Wu, S. Lan, G. Peng, X.L. Wang, H. Hahn, H. Gleiter, T. Feng, Ni-P nanoglass prepared by multi-phase pulsed electrodeposition, Mater. Res. Lett. 5 (2017) 293–299, https://doi.org/10.1080/21663831.2016.1264495.
[8] C. Wang, X. Mu, M.R. Chellali, A. Kilmametov, Y. Ivanisenko, H. Gleiter, H. Hahn, Tuning the Curie temperature of Fe90Sc10 nanoglasses by varying the volume fraction and the composition of the interfaces, Scr. Mater. 159 (2019) 109–112, https://doi.org/10.1016/j.scriptamat.2018.09.025.
[9] S.P. Singh, R. Witte, O. Clemens, A. Sarkar, L. Velasco, R. Kruk, H. Hahn, Magnetic Tb75Fe25Nanoglass for Cryogenic Permanent Magnet Undulator, ACS Appl. Nano Mater. 3 (2020) 7281–7290, https://doi.org/10.1021/acsanm.0c01674.
[10] D. Şopu, K. Albe, Y. Ritter, H. Gleiter, From nanoglasses to bulk massive glasses, Appl. Phys. Lett. 94 (2009), 191911, https://doi.org/10.1063/1.3130209.
[11] Y. Ritter, D. Sopu, H. Gleiter, K. Albe, Structure, stability and mechanical properties of internal interfaces in Cu64Zr36 nanoglasses studied by MD simulations, Acta Mater 59 (2011) 6588–6593, https://doi.org/10.1016/j.actamat.2011.07.013.
[12] S.H. Nandam, Y. Ivanisenko, R. Schwaiger, Z. Śniadecki, X. Mu, D. Wang, R. Chellali, T. Boll, A. Kilmametov, T. Bergfeldt, H. Gleiter, H. Hahn, Cu-Zr nanoglasses: Atomic structure, thermal stability and indentation properties, Acta Mater 136 (2017) 181–189, https://doi.org/10.1016/j.actamat.2017.07.001.
[13] X. Wang, F. Jiang, H. Hahn, J. Li, H. Gleiter, J. Sun, J. Fang, Sample size effects on strength and deformation mechanism of Sc75Fe25 nanoglass and metallic glass, Scr. Mater. 116 (2016) 95–99, https://doi.org/10.1016/j.scriptamat.2016.01.036.
[14] W.H. Liu, B.A. Sun, H. Gleiter, S. Lan, Y. Tong, X.L. Wang, H. Hahn, Y. Yang, J. J. Kai, C.T. Liu, Nanoscale Structural Evolution and Anomalous Mechanical Response of Nanoglasses by Cryogenic Thermal Cycling, Nano Lett 18 (2018) 4188–4194, https://doi.org/10.1021/acs.nanolett.8b01007.
[15] S. Adibi, Z.D. Sha, P.S. Branicio, S.P. Joshi, Z.S. Liu, Y.W. Zhang, A transition from localized shear banding to homogeneous superplastic flow in nanoglass, Appl. Phys. Lett. 103 (2013) 211905-5, https://doi.org/10.1063/1.4833018.
[16] I. Singh, R. Narasimhan, Y.W. Zhang, Ductility enhancement in nanoglass: role of interaction stress between flow defects, Philos. Mag. Lett. 94 (2014) 678–687, https://doi.org/10.1080/09500839.2014.961584.
[17] D. Şopu, Y. Ritter, H. Gleiter, K. Albe, Deformation behavior of bulk and nanostructured metallic glasses studied via molecular dynamics simulations, Phys. Rev. B. 83 (2011) 100202–100204, https://doi.org/10.1103/PhysRevB.83.100202.
[18] Z.D. Sha, P.S. Branicio, Q.X. Pei, Z.S. Liu, H.P. Lee, T.E. Tay, T.J. Wang, Strong and superplastic nanoglass, Nanoscale 7 (2015) 17404–17409, https://doi.org/10.1039/c5nr04740d.
[19] O. Adjaoud, K. Albe, Influence of microstructural features on the plastic deformation behavior of metallic nanoglasses, Acta Mater 168 (2019) 393–400, https://doi.org/10.1016/j.actamat.2019.02.033.
[20] O. Franke, D. Leisen, H. Gleiter, H. Hahn, Thermal and plastic behavior of nanoglasses, J. Mater. Res. 29 (2014) 1210–1216, https://doi.org/10.1557/jmr.2014.101.
[21] C. Guo, Y. Fang, F. Chen, T. Feng, Nanoindentation creep behavior of electrodeposited Ni-P nanoglass films, Intermetallics 110 (2019), 106480, https://doi.org/10.1016/j.intermet.2019.106480.
[22] S.H. Nandam, O. Adjaoud, R. Schwaiger, Y. Ivanisenko, M.R. Chellali, D. Wang, K. Albe, H. Hahn, Influence of topological structure and chemical segregation on the thermal and mechanical properties of Pd–Si nanoglasses, Acta Mater 193 (2020) 252–260, https://doi.org/10.1016/j.actamat.2020.03.021.
[23] J.I. Jang, B.G. Yoo, Y.J. Kim, J.H. Oh, I.C. Choi, H. Bei, Indentation size effect in bulk metallic glass, Scr. Mater. 64 (2011) 753–756, https://doi.org/10.1016/j.scriptamat.2010.12.036.
[24] W.W. Gerberich, N.I. Tymiak, J.C. Grunlan, M.F. Horstemeyer, M.I. Baskes, Interpretations of indentation size effects, J. Appl. Mech. 69 (2002) 433–442, https://doi.org/10.1115/1.1469004.
[25] H. Li, A. Ghosh, Y.H. Han, R.C. Bradt, The frictional component of the indentation size effect in low load microhardness testing, J. Mater. Res. 8 (1993) 1028–1032, https://doi.org/10.1557/JMR.1993.1028.
[26] W.D. Nix, H. Gao, Indentation size effects in crystalline materials: A law for strain gradient plasticity, J. Mech. Phys. Solids. 46 (1998) 411–425, https://doi.org/10.1016/S0022-5096(97)00086-0.
[27] D.C.C. Lam, A.C.M. Chong, Model and experiments on strain gradient hardening in metallic glass, Mater. Sci. Eng. A. 318 (2001) 313–319, https://doi.org/10.1016/S0921-5093(01)01329-6.
[28] F. Yang, K. Geng, P.K. Liaw, G. Fan, H. Choo, Deformation in a Zr57Ti5Cu20Ni8Al10 bulk metallic glass during nanoindentation, Acta Mater 55 (2007) 321–327, https://doi.org/10.1016/j.actamat.2006.06.063.
[29] N.V. Steenberge, J. Sort, A. Concustell, J. Das, S. Scudino, S. Suriñach, J. Eckert, M. D. Baró, Dynamic softening and indentation size effect in a Zr-based bulk glass-forming alloy, Scr. Mater. 56 (2007) 605–608, https://doi.org/10.1016/j.scriptamat.2006.12.014.
[30] N. Li, K.C. Chan, L. Liu, The indentation size effect in Pd40Cu30Ni10P20 bulk metallic glass, J. Phys. D. Appl. Phys. 41 (2008), 155415, https://doi.org/10.1088/0022-3727/41/15/155415.
[31] N. Li, L. Liu, K.C. Chan, Deformation behavior and indentation size effect in amorphous and crystallized Pd40Cu30Ni10P20 alloy, J. Mater. Res. 24 (2009) 1693–1699, https://doi.org/10.1557/jmr.2009.0222.
[32] F. Xue, F. Wang, P. Huang, T.J. Lu, K.W. Xu, Structural inhomogeneity and strain rate dependent indentation size effect in Zr-based metallic glass, Mater. Sci. Eng. A. 655 (2016) 373–378, https://doi.org/10.1016/j.msea.2015.12.083.
[33] W.J. Wright, R. Saha, W.D. Nix, Deformation mechanisms of the Zr40Ti14Ni10Cu12Be24, Mater Trans JIM 42 (2001) 642–649, https://doi.org/10.2320/matertrans.42.642.
[34] Y. Huang, J. Shen, Y. Sun, J. Sun, Indentation size effect of hardness of metallic glasses, Mater. Des. 31 (2010) 1563–1566, https://doi.org/10.1016/j.matdes.2009.09.046.
[35] J.J. Pang, M.J. Tan, K.M. Liew, C. Shearwood, Nanoindentation study of size effect and loading rate effect on mechanical properties of a thin film metallic glass Cu49.3Zr50.7, Phys. B 407 (2012) 340–346, https://doi.org/10.1016/j.physb.2011.10.050.
[36] A. Rauf, C.Y. Guo, Y.N. Fang, Z. Yu, B.A. Sun, T. Feng, Binary Cu-Zr thin film metallic glasses with tunable nanoscale structures and properties, J. Non. Cryst. Solids. 498 (2018) 95–102, https://doi.org/10.1016/j.jnoncrysol.2018.06.015.

[37] A. Sharma, S.H. Nandam, H. Hahn, K.E. Prasad, Effect of Structural Relaxation on the Indentation Size Effect and Deformation Behavior of Cu–Zr–Based Nanoglasses, Front. Mater. 8 (2021) 1–10, https://doi.org/10.3389/fmats.2021.676764.
[38] S.S. Hirmukhe, K.E. Prasad, I. Singh, Investigation of pressure sensitive plastic flow in nanoglasses from finite element simulations, Scr. Mater. 180 (2020) 45–50, https://doi.org/10.1016/j.scriptamat.2020.01.022.
[39] W.C. Oliver, G.M. Pharr, Measurement of hardness and elastic modulus by instrumented indentation: Advances in understanding and refinements to methodology, J. Mater. Res. 19 (2004) 3–20, https://doi.org/10.1557/jmr.2004.19.1.3.
[40] L. Anand, C. Su, A theory for amorphous viscoplastic materials undergoing finite deformations, with application to metallic glasses, J. Mech. Phys. Solids. 53 (2005) 1362–1396, https://doi.org/10.1016/j.jmps.2004.12.006.
[41] C. Su, L. Anand, Plane strain indentation of a Zr-based metallic glass: Experiments and numerical simulation, Acta Mater 54 (2006) 179–189, https://doi.org/10.1016/j.actamat.2005.08.040.
[42] ABAQUS/Standard, Theory Manual, Hibbit Karlsson and Sorenson Inc., RI, 1996.
[43] P. Tandaiya, R. Narasimhan, U. Ramamurty, Mode I crack tip fields in amorphous materials with application to metallic glasses, Acta Mater 55 (2007) 6541–6552, https://doi.org/10.1016/j.actamat.2007.08.017.
[44] P. Tandaiya, U. Ramamurty, R. Narasimhan, On numerical implementation of an isotropic elastic-viscoplastic constitutive model for bulk metallic glasses, Model. Simul. Mater. Sci. Eng. 19 (2011), 015002, https://doi.org/10.1088/0965-0393/19/1/015002.
[45] M.N.M. Patnaik, R. Narasimhan, U. Ramamurty, Spherical indentation response of metallic glasses, Acta Mater 52 (2004) 3335–3345, https://doi.org/10.1016/j.actamat.2004.03.028.
[46] J.C. Lee, K.W. Park, K.H. Kim, E. Fleury, B.J. Lee, M. Wakeda, Y. Shibutani, Origin of the plasticity in bulk amorphous alloys, J. Mater. Res. 22 (2007) 3087–3097, https://doi.org/10.1557/jmr.2007.0382.
[47] F.C. Li, T.Y. Wang, Q.F. He, B.A. Sun, C.Y. Guo, T. Feng, Y. Yang, Micromechanical mechanism of yielding in dual nano-phase metallic glass, Scr. Mater. 154 (2018) 186–191, https://doi.org/10.1016/j.scriptamat.2018.05.050.
[48] P. Tandaiya, U. Ramamurty, R. Narasimhan, Mixed mode (I and II) crack tip fields in bulk metallic glasses, J. Mech. Phys. Solids. 57 (2009) 1880–1897, https://doi.org/10.1016/j.jmps.2009.07.006.
[49] S.S. Hirmukhe, K.E. Prasad, I. Singh, Finite element analysis of tensile deformation of nanoglass-metallic glass laminate composites, Comput. Mater. Sci. 161 (2019) 83–92, https://doi.org/10.1016/j.commatsci.2019.01.031.
[50] A. Sharma, S.H. Nandam, H. Hahn, K.E. Prasad, On the differences in shear band characteristics between a binary Pd-Si metallic and nanoglass, Scr. Mater. 191 (2021) 17–22, https://doi.org/10.1016/j.scriptamat.2020.09.009.
[51] R. Bhowmick, R. Raghavan, K. Chattopadhyay, U. Ramamurty, Plastic flow softening in a bulk metallic glass, Acta Mater 54 (2006) 4221–4228, https://doi.org/10.1016/j.actamat.2006.05.011.
[52] K.E. Prasad, U. Ramamurty, Effect of temperature on the plastic zone size and the shear band density in a bulk metallic glass, Mater. Sci. Eng. A. 535 (2012) 48–52, https://doi.org/10.1016/j.msea.2011.12.040.
[53] S.D. Fang, L. Li, Y.D. Liu, L.M. Wang, R.P. Liu, Heterogeneous microstructure of $Zr_{46}Cu_{46}Al_8$ nanoglasses studied by quantifying glass-glass interfaces, J. Non. Cryst. Solids. 546 (2020), 120265, https://doi.org/10.1016/j.jnoncrysol.2020.120265.
[54] S.D. Fang, L. Qi, L. Wang, S. Pan, M. Ma, X. Zhang, G. Li, R. Liu, Atomic structure of shear bands in $Cu_{64}Zr_{36}$ metallic glasses studied by molecular dynamics simulations, Acta Mater 95 (2015) 236–243, https://doi.org/10.1016/j.actamat.2015.05.047.
[55] K. Tao, J.C. Qiao, Q.F. He, K.K. Song, Y. Yang, Revealing the structural heterogeneity of metallic glass: Mechanical spectroscopy and nanoindentation experiments, Int. J. Mech. Sci. 201 (2021), https://doi.org/10.1016/j.ijmecsci.2021.106469.
[56] C.A. Schuh, A.C. Lund, T.G. Nieh, New regime of homogeneous flow in the deformation map of metallic glasses: Elevated temperature nanoindentation experiments and mechanistic modeling, Acta Mater 52 (2004) 5879–5891, https://doi.org/10.1016/j.actamat.2004.09.005.
[57] M. Rodríguez, J.M. Molina-Aldareguía, C. González, J. Llorca, Determination of the mechanical properties of amorphous materials through instrumented nanoindentation, Acta Mater 60 (2012) 3953–3964, https://doi.org/10.1016/j.actamat.2012.03.027.
[58] F. Spaepen, A microscopic mechanism for steady state inhomogeneous flow in metallic glasses, Acta Metall 25 (1977) 407–415, https://doi.org/10.1016/0001-6160(77)90232-2.
[59] A.S. Argon, Plastic deformation Plastic deformation in metallic glasses, Acta Metall 27 (1979) 47–58, https://doi.org/10.1016/0001-6160(79)90055-5.
[60] A. Concustell, J. Sort, G. Alcalá, S. Mato, A. Gebert, J. Eckert, M.D. Baró, Plastic deformation and mechanical softening of Pd40 Cu30Ni10P20 bulk metallic glass during nanoindentation, J. Mater. Res. 20 (2005) 2719–2725, https://doi.org/10.1557/JMR.2005.0331.
[61] P. Thamburaja, Length scale effects on the shear localization process in metallic glasses: A theoretical and computational study, J. Mech. Phys. Solids. 59 (2011) 1552–1575, https://doi.org/10.1016/j.jmps.2011.04.018.
[62] I. Singh, R. Narasimhan, Notch sensitivity in nanoscale metallic glass specimens: Insights from continuum simulations, J. Mech. Phys. Solids. 86 (2016) 53–69, https://doi.org/10.1016/j.jmps.2015.10.001.